

Dense media radiative transfer theory based on quasicrystalline approximation with applications to passive microwave remote sensing of snow

Leung Tsang,¹ Chi-Te Chen,¹ Alfred T. C. Chang,²
Jianjun Guo,¹ and Kung-Hau Ding³

Abstract. Dense media radiative transfer (DMRT) equations based on quasicrystalline approximation (QCA) for densely distributed moderate size particles are developed. We first compute the effective propagation constant and coherent transmission into a dense medium on the basis of the generalized Lorentz-Lorenz law and the generalized Ewald-Oseen extinction theorem. The absorption coefficient of the dense media is then calculated. The distorted Born approximation is next applied to a thin layer to determine the bistatic scattering coefficients and the scattering coefficient. The phase matrix in DMRT is then obtained as bistatic scattering coefficient per unit volume. The model is applied to multiple sizes and for sticky particles. Numerical results are illustrated for extinction and brightness temperatures in passive remote sensing using typical parameters in snow terrain. The QCA-based DMRT is also used to compare with satellite Special Sensor Microwave Imager (SSM/I) brightness temperatures for four channels at 19 and 37 GHz with vertical and horizontal polarizations and for two snow seasons. It shows reasonable agreement to snow depth of 1 m.

1. Introduction

Wave propagation and scattering in densely packed media are important issues in the volume scattering problem of geophysical media and composite materials. In densely packed media the particles do not scatter independently. The correlation between particles has to be taken into account. This has been validated in laboratory experiments [Ishimaru and Kuga, 1982] and Monte Carlo solutions of Maxwell's equations [Tsang *et al.*, 1992; Lu *et al.*, 1995]. Therefore the quasicrystalline approximation (QCA) and the quasicrystalline approximation with coherent potential (QCA-CP), which account for the pair distribution function of the particle positions and coherent wave interactions, have been used [Tsang *et al.*, 1985]. The Percus-Yevick equation is used to describe the pair distribution functions [Tsang *et al.*, 1985]. The

advantages of the QCA and QCA-CP are as follows: (1) The scattering results compare well with the Monte Carlo simulations of exact solutions of Maxwell's equations [Tsang *et al.*, 1992] of randomly distributed finite size spheres, and (2) the Percus-Yevick pair distribution functions of multiple particle sizes also compare well with Monte Carlo simulations of pair distribution functions of particles without interparticle forces [Ding *et al.*, 1992]. For the second moment a correlated ladder approximation was used on Bethe-Salpeter equation [Tsang, 1992]. It was shown that QCA-CP and the correlated ladder approximation obey energy conservation. These two sets of approximations were then used to derive the dense media radiative transfer equations [Tsang, 1992]. However, the QCA-CP is a nonlinear approximation, and the solution has been limited to small particles. Thus for the previous dense media radiative transfer (DMRT) model that was derived from QCA-CP and correlated ladder approximation, the Rayleigh phase function was obtained in the derivations.

In this paper, we develop a dense media radiative transfer theory for moderate-size particles based on QCA rather than QCA-CP. The QCA is used to calculate the effective propagation constant and the coherent transmission into a dense medium. Higher-order multipole effects are included so that the model

¹ Department of Electrical Engineering, University of Washington, Seattle.

² Hydrological Sciences Branch, NASA Goddard Space Flight Center, Greenbelt, Maryland.

³ Air Force Research Laboratory, Sensors Directorate, Electromagnetics Technology Division, Electromagnetic Scattering Branch, Hanscom Air Force Base, Massachusetts.

is applicable to moderate-size particles. From the coherent exciting field we calculate the absorption coefficient. We then use the distorted Born approximation to calculate the incoherent bistatic scattering coefficients and the scattering coefficient by integrating over the bistatic scattering coefficients over 4π solid angles. The phase matrix of DMRT is then calculated from the bistatic scattering coefficients per unit volume. The extinction coefficient is calculated by adding the absorption coefficient and the scattering coefficient to assure energy conservation. The results of extinction coefficient and DMRT are illustrated for densely packed particles of multiple sizes and also for sticky particles. The Percus-Yevick pair distribution functions are used for both cases. The sticky particle cases are used to model particles that have interparticle force and tend to adhere to form aggregates [Ding *et al.*, 1994; Zurk, 1995]. We illustrate the solutions of DMRT by calculating the brightness temperatures in passive remote sensing at 19 and 37 GHz for vertical and horizontal polarizations using typical parameters in snow terrains. Salient features of the numerical results of the sticky particles are as follows: (1) The scattering is higher than independent scattering at low frequency and smaller than independent scattering at high frequency. This behavior is different from dense media without interparticle forces. (2) The brightness temperatures at 37 GHz saturate at moderately small depth. (3) The brightness temperature difference between 19 and 37 GHz is linear with snow depth for small snow depth and small grain size but becomes nonlinear for large snow depth and large grain size.

The DMRT theory is also used to compare with Special Sensor Microwave Imager (SSM/I) measurements of all four channels (19V, 19H, 37V, and 37H, where V and H refer to vertical and horizontal polarization, respectively) as a function of time for two entire snow seasons. Comparisons indicate that the observed SSM/I features can be accounted for by the sticky particle scattering model.

In section 2, we describe the QCA theory for densely packed particles of moderate sizes, the QCA results for the coherent transmission coefficients into dense media, and the absorption coefficients. The equations that are used to compute the effective propagation constants, scattering coefficients, and absorption coefficients are listed. In section 3, we derive the phase matrix and scattering coefficients by using the distorted Born approximation with QCA. The DMRT equations are then derived. In section 4,

we describe the pair distribution functions and structure factors of particles of multiple sizes and for sticky particles. The theoretical results of DMRT to calculate brightness temperatures are illustrated numerically in section 5. In section 6, comparisons of the brightness temperatures of DMRT are made with SSM/I snow brightness temperature measurements.

2. Quasicrystalline Approximation Formulation

Consider a medium consisting of N particles centered at $\mathbf{r}_1, \mathbf{r}_2, \dots, \mathbf{r}_N$. Let the incident wave be impinging in the direction of \mathbf{k}_i . The Foldy-Lax multiple-scattering equation can be written in matrix form as

$$\mathbf{w}^{(j)} = \sum_{\substack{l=1 \\ l \neq j}}^N \boldsymbol{\sigma}(k\mathbf{r}_j\mathbf{r}_l) \mathbf{T}^{(l)} \mathbf{w}^{(l)} + e^{i(\mathbf{k}_i \cdot \mathbf{r}_j)} \mathbf{a}_{\text{inc}}, \quad (1)$$

where $\mathbf{w}^{(j)}$ and $\mathbf{w}^{(l)}$ are the exciting field coefficients of the j th particle and the l th particle, respectively, $\mathbf{T}^{(l)}$ is the T matrix of the l th particle, and \mathbf{a}_{inc} is the incident field coefficient. Equation (1) can be interpreted as the field exciting the j th particle, which is the sum of incident wave and the scattered wave from all other particles. The matrix $\boldsymbol{\sigma}(k\mathbf{r}_j\mathbf{r}_l)$ is the matrix that describes the vector translation formula transforming spherical waves centered at \mathbf{r}_l to spherical waves centered at \mathbf{r}_j . By taking the conditional average by holding position \mathbf{r}_j fixed, we have

$$\begin{aligned} \mathbf{w}(\mathbf{r}_j) &= E_j(\mathbf{w}^{(j)}) \\ &= \sum_{\substack{l=1 \\ l \neq j}}^N \int d\mathbf{r}_l \boldsymbol{\sigma}(k\mathbf{r}_j\mathbf{r}_l) p(\mathbf{r}_l|\mathbf{r}_j) \mathbf{T}^{(l)} E_{lj}(\mathbf{w}^{(l)}) + e^{i(\mathbf{k}_i \cdot \mathbf{r}_j)} \mathbf{a}_{\text{inc}}, \end{aligned} \quad (2)$$

where E_j is the conditional average given the position and state of the j th particle, $p(\mathbf{r}_l|\mathbf{r}_j)$ is the conditional probability of finding the l th particle at \mathbf{r}_l given the j th particle at \mathbf{r}_j , and E_{lj} is the conditional average given the properties and positions of particles l and j .

Based on the quasicrystalline approximation,

$$E_{lj}(\mathbf{w}^{(l)}) = E_l(\mathbf{w}^{(l)}) \equiv \mathbf{w}(\mathbf{r}_l). \quad (3)$$

Therefore the averaged exciting field under the quasicrystalline approximation obeys the following equation:

$$\mathbf{w}^{(s_l)}(\mathbf{r}_j) = \sum_{s_l=1}^L n_{s_l} \int_{V_{ij}} d\mathbf{r}_l g_{s_l s_j}(\mathbf{r}_l - \mathbf{r}_j) \boldsymbol{\sigma}(k\mathbf{r}_j \mathbf{r}_l) \mathbf{T}^{(l)} \mathbf{w}^{(s_l)}(\mathbf{r}_l) + e^{i(\mathbf{k}_d \cdot \mathbf{r}_j)} \mathbf{a}_{\text{inc}}, \quad (4)$$

where s_l is the species, under which we assume that there are L species of particles in the medium, n_{s_l} is the number of particles per unit volume of L species, $\mathbf{w}^{(s_l)}(\mathbf{r}_j)$ is the conditional average of the exciting field of particles at \mathbf{r}_j of species s_j , $\mathbf{T}^{(l)}$ is the matrix representation of the \mathbf{T} matrix of species s_l , and $g_{s_l s_j}(\mathbf{r}_l - \mathbf{r}_j)$ is the cross-pair distribution function of two species s_l and s_j . The \mathbf{a}_{inc} is the column matrix representing the coefficient of the incident wave when expanded into spherical waves.

The integral equation in (4) can be solved by using vector spherical wave expansions. They lead into two sets of equations, the Lorentz-Lorenz law and the Ewald-Oseen extinction theorem [Tsang and Kong, 1992]. The conditional averaged exciting field coefficients obey the following homogeneous system of equations (Lorentz-Lorenz law).

Let $\mathbf{w}^{(s_l)}(\mathbf{r}_j)$ be expanded into vector spherical waves with $Y_{\nu}^{(s_l)(M)}$ and $Y_{\nu}^{(s_l)(N)}$ as coefficients where $\nu = 1, 2, \dots$ and (M) and (N) represent the \mathbf{M} and \mathbf{N} vector spherical waves, respectively.

$$Y_{\nu}^{(s_l)(M)} = -2\pi \sum_{s_l=1}^L n_{s_l} \sum_{n,p} (2n+1) S_p(k, K | R_{s_l s_l}) \cdot \{a(1, n|-1, \nu|p) A(n, \nu, p) T_n^{(s_l)(M)} Y_n^{(s_l)(M)} + a(1, n|-1, \nu|p, p-1) B(n, \nu, p) T_n^{(s_l)(N)} Y_n^{(s_l)(N)}\}, \quad (5)$$

$$Y_{\nu}^{(s_l)(N)} = -2\pi \sum_{s_l=1}^L n_{s_l} \sum_{n,p} (2n+1) S_p(k, K | R_{s_l s_l}) \cdot \{a(1, n|-1, \nu|p, p-1) B(n, \nu, p) T_n^{(s_l)(M)} Y_n^{(s_l)(M)} + a(1, n|-1, \nu|p) A(n, \nu, p) T_n^{(s_l)(N)} Y_n^{(s_l)(N)}\}. \quad (6)$$

In (5) and (6),

$$S_p(k, K | R_{s_l s_l}) = -\frac{R_{s_l s_l}^2}{K^2 - k^2} \cdot [kh'_p(kR_{s_l s_l}) j_p(KR_{s_l s_l}) - Kh_p(kR_{s_l s_l}) j'_p(kR_{s_l s_l})] + \int_{R_{s_l s_l}}^{\infty} dr r^2 [g_{s_l s_l}(r) - 1] h_p(kr) j_p(Kr), \quad (7)$$

where $A(n, \nu, p)$ and $B(n, \nu, p)$ are the coefficients defined by Tsang *et al.* [1985, p. 496] and $a(1, n|-1, \nu|p)$ and $a(1, n|-1, \nu|p, p-1)$ are in terms of Wigner $3j$ symbols defined by Tsang *et al.* [1985, pp. 449–450]. $T_n^{(M)}$ and $T_n^{(N)}$ are the Mie scattering \mathbf{T} matrix coefficients defined by Tsang *et al.* [1985, p. 189], and $K = K' + iK''$ is the effective propagation constant. Here j_p and j'_p are the spherical Bessel function and its derivative, and h_p and h'_p are the spherical Hankel function and its derivative. The ratios of exciting field coefficients $Y_{\nu}^{(s_l)(M)}$ and $Y_{\nu}^{(s_l)(N)}$ are determined by setting the determinant of (5) and (6) equal to zero. The determinant equation gives the solution for the effective propagation constant K . They can be solved numerically by using Muller's method to search the root K . Therefore the value of $Y_{\nu}^{(s_l)(M)}$ and $Y_{\nu}^{(s_l)(N)}$ can be determined within a single constant. The effective propagation constant K is complex, $K = K' + iK''$, and the extinction rate is $\kappa_e = 2K''$. In principle, both K' and K'' can be computed by the Lorentz-Lorenz law. However, since $K' \gg K''$, K'' calculated in this manner may not have the desired accuracy. Also, the imaginary part K'' is affected by the sticky particle pair distribution functions that have sharp peaks that may be difficult to evaluate numerically. Furthermore, QCA combined with distorted Born approximation may not conserve energy. To assure energy conservation, we proceed as follows. We use the real part K' as calculated from (5) and (6) of Lorentz-Lorenz law. We also use the relative values of $Y_{\nu}^{(s_l)}$ as determined by (5) and (6). For the single constant it is determined by Ewald-Oseen extinction theorem. The generalized Ewald-Oseen extinction theorem is obtained by balancing the incident wave term and the term of the same phase dependence that is a result of the integral in (4). We then use the coherent exciting field to calculate the absorption coefficient. The distorted Born approximation is applied to calculate bistatic scattering coefficients and the scattering coefficient. Then, the extinction coefficient is calculated by the addition of absorption and scattering coefficients.

To calculate the absorption coefficient, we will consider normal incidence upon the layer of dense medium. For normal incidence in the body frame, without loss of arbitrariness, we then choose the vertical polarization incidence. The Ewald-Oseen extinction theorem gives rise to the following inhomogeneous equation:

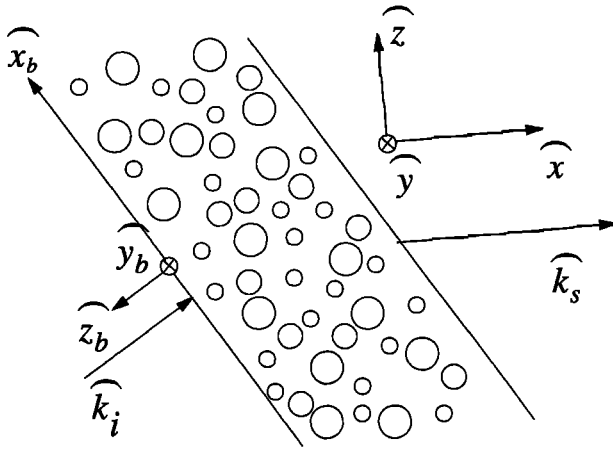


Figure 1. Body frame and principal frame of a thin layer. Calculation of the phase matrix for QCA and distorted Born approximation.

$$\begin{aligned}
 & \sum_{s_i=1}^L \sum_n n_s i \frac{(2n+1)}{n(n+1)} \\
 & \cdot \left\{ -T_n^{(s_i)(M)} Y_n^{(s_i)(M)(V)} \frac{P_n^1[\cos(\theta_i - \theta_t)]}{|\sin(\theta_i - \theta_t)|} \right. \\
 & + T_n^{(s_i)(N)} Y_n^{(s_i)(N)(V)} \left[\cos(\theta_i - \theta_t) \frac{P_n^1[\cos(\theta_i - \theta_t)]}{|\sin(\theta_i - \theta_t)|} \right. \\
 & \left. \left. + n(n+1)P_n[\cos(\theta_i - \theta_t)] \right] \right\} \\
 & = -\frac{(K_z - k_{iz})k_{iz}k}{2\pi}, \quad (8)
 \end{aligned}$$

where P_n^1 is the associated Legendre polynomial of n th order and degree 1 and P_n is the Legendre polynomial. θ_i and θ_t are the incident and transmitted angles, respectively. K_z and k_{iz} are the z component of the effective propagation constant K and the incident wave number. The additional superscript (V) denoted the vertically polarized case. The set of coefficients $Y_n^{(s_i)(M)(V)}$ and $Y_n^{(s_i)(N)(V)}$ have been determined to within one arbitrary constant by the generalized Lorentz-Lorenz law of (5) and (6). Thus (8) provides the last equation that determines all those coefficients uniquely.

The coherent reflection coefficient is

$$R = \sum_{s_j=1}^L \frac{2\pi n_s i}{k k_{iz}(K_z + k_{iz})} \sum_n (-1)^n \frac{(2n+1)}{n(n+1)}$$

$$\begin{aligned}
 & \cdot \left(T_n^{(s_j)(M)} Y_n^{(s_j)(M)(V)} \frac{P_n^1[\cos(\theta_i + \theta_t)]}{\sin(\theta_i + \theta_t)} \right. \\
 & + T_n^{(s_j)(N)} Y_n^{(s_j)(N)(V)} \{ n(n+1)P_n[\cos(\theta_i + \theta_t)] \\
 & \left. + \cot(\theta_i + \theta_t)P_n^1[\cos(\theta_i + \theta_t)] \} \right). \quad (9)
 \end{aligned}$$

The absorption coefficient can be calculated by using the coherent exciting field on a particle $\mathbf{w}^{(s_j)}(\mathbf{r}_j)$ as solved by QCA. It follows that

$$\begin{aligned}
 \kappa_a &= \frac{2\pi}{k^2 |1-R|^2} \sum_{s_j=1}^L n_s \sum_n (2n+1) \\
 & \cdot [|Y_n^{(s_j)(M)(V)}|^2 (-\text{Re } T_n^{(s_j)(M)} - |T_n^{(s_j)(M)}|^2) \\
 & + |Y_n^{(s_j)(N)(V)}|^2 (-\text{Re } T_n^{(s_j)(N)} - |T_n^{(s_j)(N)}|^2)]. \quad (10)
 \end{aligned}$$

To develop DMRT, we consider an incident wave normally impinging upon a thin layer of medium. The body frame $\hat{\mathbf{x}}_b, \hat{\mathbf{y}}_b, \hat{\mathbf{z}}_b$ and the principal frame $\hat{\mathbf{x}}, \hat{\mathbf{y}}, \hat{\mathbf{z}}$ are defined in Figure 1.

In the body frame the incident angle is $\theta_i = 0^\circ$. Thus the transmitted angle of the coherent wave has $\theta_t = 0^\circ$. For normal incidence we let incident wave be vertical polarized without loss of generality. Equation (8) can then be further simplified as

$$\begin{aligned}
 & \sum_{s_i=1}^L \sum_n n_s i \frac{(2n+1)}{2} [T_n^{(s_i)(M)} Y_n^{(s_i)(M)(V)} + T_n^{(s_i)(N)} Y_n^{(s_i)(N)(V)}] \\
 & = -\frac{(K - k)k^2}{2\pi}. \quad (11)
 \end{aligned}$$

The coherent reflection coefficient for normal incidence is

$$\begin{aligned}
 R &= \sum_{s_j=1}^L \frac{2\pi n_s i}{k^2(K+k)} \sum_n (-1)^n \frac{(2n+1)}{2} \\
 & \cdot [-T_n^{(s_j)(M)} Y_n^{(s_j)(M)(V)} + T_n^{(s_j)(N)} Y_n^{(s_j)(N)(V)}]. \quad (12)
 \end{aligned}$$

Note that the ratio of Y_n is determined by Lorentz-Lorenz law. The Ewald-Oseen extinction theorem of (4) then uniquely solves all the Y_n coefficients. Equation (11) provides the solutions to the $Y_n^{(s_j)(M)}$ and $Y_n^{(s_j)(N)}$ coefficients.

3. Phase Matrix

To include higher-order multiple-scattering effects for the incoherent wave, the radiative transfer type of equations are used. The phase matrix elements are derived by using quasicrystalline approximation (QCA) and distorted Born approximation for a thin layer and then inserted into radiative transfer equations. By using QCA and the distorted Born approximation the bistatic scattering coefficients can be calculated.

Consider an incident wave impinging upon a volume of dense medium consisting of spheres of moderate sizes with size distributions (Figure 1). The incident direction is $\hat{\mathbf{k}}_i$, and the polarization directions are $\hat{\mathbf{v}}_i$ and $\hat{\mathbf{h}}_i$.

$$\hat{\mathbf{k}}_i = \sin \theta_i \hat{\mathbf{x}} + \cos \theta_i \hat{\mathbf{z}}, \quad (13)$$

$$\hat{\mathbf{v}}_i = \cos \theta_i \hat{\mathbf{x}} - \sin \theta_i \hat{\mathbf{z}}, \quad (14)$$

$$\hat{\mathbf{h}}_i = \hat{\mathbf{y}}. \quad (15)$$

We first calculate the phase matrix in the body frame. Assume a body frame of the medium such that $\hat{\mathbf{z}}_b$ is pointing at the negative $\hat{\mathbf{k}}_i$ direction, $\hat{\mathbf{z}}_b = -\hat{\mathbf{k}}_i$. Further, let the body frame $\hat{\mathbf{y}}_b = \hat{\mathbf{y}}$, so that $\hat{\mathbf{x}}_b = -\cos \theta_i \hat{\mathbf{x}} + \sin \theta_i \hat{\mathbf{z}}$. We also let the vertical polarization in the body frame be

$$\hat{\mathbf{v}}_{ib} = -\hat{\mathbf{x}}_b = -\hat{\mathbf{v}}_i, \quad (16)$$

$$\hat{\mathbf{h}}_{ib} = \hat{\mathbf{y}}_b = \hat{\mathbf{h}}_i. \quad (17)$$

For incoherent scattered wave, we can write the scattered wave in the body frame using the three orthonormal vectors

$$\hat{\mathbf{k}}_s = \sin \theta_{bs} \cos \phi_{bs} \hat{\mathbf{x}}_b + \sin \theta_{bs} \sin \phi_{bs} \hat{\mathbf{y}}_b + \cos \theta_{bs} \hat{\mathbf{z}}_b, \quad (18)$$

$$\hat{\mathbf{v}}_{bs} = \cos \theta_{bs} \cos \phi_{bs} \hat{\mathbf{x}}_b + \cos \theta_{bs} \sin \phi_{bs} \hat{\mathbf{y}}_b - \sin \theta_{bs} \hat{\mathbf{z}}_b, \quad (19)$$

$$\hat{\mathbf{h}}_{bs} = -\sin \phi_{bs} \hat{\mathbf{x}}_b + \cos \phi_{bs} \hat{\mathbf{y}}_b, \quad (20)$$

where $\hat{\mathbf{k}}_s$ denotes the scattered direction and $\hat{\mathbf{v}}_{bs}$ and $\hat{\mathbf{h}}_{bs}$ are the polarization vectors in the body frame.

Since in the body frame the wave is normally impinging upon the dense media $\theta_{bt} = 0$, the bistatic scattering coefficients depend on $W_{\beta\alpha}^{(s)}(\theta_{bs}, \phi_{bs}; \pi - \theta_{bt}, \phi_{bt})$ [Tsang and Kong, 1992]:

$$\begin{aligned} \gamma_{\beta\alpha}(\theta_{bs}, \phi_{bs}; \pi - \theta_{bt}, \phi_{bt}) = & \frac{4\pi}{k^2 \cos \theta_{bt}} \frac{F_d}{2K_z''} \\ & \cdot \left\{ \sum_{s_j=1}^L n_{s_j} |W_{\beta\alpha}^{(s_j)}(\theta_{bs}, \phi_{bs}; \pi - \theta_{bt}, \phi_{bt})|^2 \right. \\ & + \sum_{s_j=1}^L \sum_{s_l=1}^L n_{s_j} n_{s_l} W_{\beta\alpha}^{(s_j)}(\theta_{bs}, \phi_{bs}; \pi - \theta_{bt}; \phi_{bt}) W_{\beta\alpha}^{(s_l)*} \\ & \cdot (\theta_{bs}, \phi_{bs}; \pi - \theta_{bt}, \phi_{bt}) (2\pi)^3 H_{s_j s_l}(|\mathbf{k}_{bs} - \text{Re } \mathbf{K}_d|) \left. \right\}. \end{aligned} \quad (21)$$

$H_{s_j s_l}$ is the structure factor which is the Fourier transform of $g_{s_j s_l}(\mathbf{r}) - 1$,

$$H_{s_j s_l}(\mathbf{p}) = \frac{1}{(2\pi)^3} \int_{-\infty}^{\infty} d\mathbf{r} e^{-i\mathbf{p} \cdot \mathbf{r}} [g_{s_j s_l}(\mathbf{r}) - 1]. \quad (22)$$

The argument of $H_{s_j s_l}$ in (21) is

$$\begin{aligned} |\mathbf{k}_{bs} - \text{Re } \mathbf{K}_d| = & |k \sin \theta_{bs} \cos \phi_{bs} \hat{\mathbf{x}} \\ & + k \sin \theta_{bs} \sin \phi_{bs} \hat{\mathbf{y}} + k \cos \theta_{bs} \hat{\mathbf{z}} + K' \hat{\mathbf{z}}| \\ = & \sqrt{k^2 \sin^2 \theta_{bs} + (k \cos \theta_{bs} + K')^2}; \end{aligned} \quad (23)$$

we then have

$$W_{VV}^{(s)}(\theta_{bs}, \phi_{bs}; \pi, 0) = \cos \phi_{bs} w_V^{(s)}(\theta_{bs}), \quad (24)$$

$$W_{VH}^{(s)}(\theta_{bs}, \phi_{bs}; \pi, 0) = -\sin \phi_{bs} w_V^{(s)}(\theta_{bs}), \quad (25)$$

$$W_{HV}^{(s)}(\theta_{bs}, \phi_{bs}; \pi, 0) = \sin \phi_{bs} w_H^{(s)}(\theta_{bs}), \quad (26)$$

$$W_{HH}^{(s)}(\theta_{bs}, \phi_{bs}; \pi, 0) = \cos \phi_{bs} w_H^{(s)}(\theta_{bs}), \quad (27)$$

where

$$\begin{aligned} w_V^{(s)}(\theta_{bs}) = & \sum_n \frac{(2n+1)}{n(n+1)} \{ P_n'(-\cos \theta_{bs}) T_n^{(s)(M)} Y_n^{(s)(M)} \\ & + T_n^{(s)(N)} Y_n^{(s)(N)} [\cos \theta_{bs} P_n'(-\cos \theta_{bs}) \\ & + n(n+1) P_n(-\cos \theta_{bs})] \}, \end{aligned} \quad (28)$$

$$\begin{aligned} w_H^{(s)}(\theta_{bs}) = & \sum_n \frac{(2n+1)}{n(n+1)} \{ T_n^{(s)(M)} Y_n^{(s)(M)} \\ & \cdot [\cos \theta_{bs} P_n'(-\cos \theta_{bs}) + n(n+1) P_n(-\cos \theta_{bs})] \\ & + T_n^{(s)(N)} Y_n^{(s)(N)} P_n'(-\cos \theta_{bs}) \}. \end{aligned} \quad (29)$$

The phase matrix is the bistatic scattering cross section per unit volume. In the body frame it can be written as

$$P_{v_b v_b}(\theta_{bs}, \phi_{bs}; \pi, 0) = \frac{1}{|1-R|^2} \frac{\cos^2 \phi_{bs}}{k^2} \cdot \left\{ \sum_{s_j=1}^L n_{s_j} |w_V^{(s_j)}(\theta_{bs})|^2 + \sum_{s_j=1}^L \sum_{s_l=1}^L n_{s_j} n_{s_l} w_V^{(s_j)}(\theta_{bs}) \cdot w_V^{(s_l)*}(\theta_{bs}) (2\pi)^3 H_{s_j s_l}(|\mathbf{k}_{bs} - \text{Re } \mathbf{K}_d|) \right\}. \quad (30)$$

Similarly,

$$P_{h_b v_b}(\theta_{bs}, \phi_{bs}; \pi, 0) = \frac{1}{|1-R|^2} \frac{\sin^2 \phi_{bs}}{k^2} \cdot \left\{ \sum_{s_j=1}^L n_{s_j} \left| w_H^{(s_j)}(\theta_{bs}) \right|^2 + \sum_{s_j=1}^L \sum_{s_l=1}^L n_{s_j} n_{s_l} w_H^{(s_j)}(\theta_{bs}) \cdot w_H^{(s_l)*}(\theta_{bs}) (2\pi)^3 H_{s_j s_l}(|\mathbf{k}_{bs} - \text{Re } \mathbf{K}_d|) \right\}, \quad (31)$$

$$P_{v_b h_b}(\theta_{bs}, \phi_{bs}; \pi, 0) = \frac{1}{|1-R|^2} \frac{\sin^2 \phi_{bs}}{k^2} \cdot \left\{ \sum_{s_j=1}^L n_{s_j} \left| w_V^{(s_j)}(\theta_{bs}) \right|^2 + \sum_{s_j=1}^L \sum_{s_l=1}^L n_{s_j} n_{s_l} w_V^{(s_j)}(\theta_{bs}) \cdot w_V^{(s_l)*}(\theta_{bs}) (2\pi)^3 H_{s_j s_l}(|\mathbf{k}_{bs} - \text{Re } \mathbf{K}_d|) \right\}, \quad (32)$$

$$P_{h_b h_b}(\theta_{bs}, \phi_{bs}; \pi, 0) = \frac{1}{|1-R|^2} \frac{\cos^2 \phi_{bs}}{k^2} \cdot \left\{ \sum_{s_j=1}^L n_{s_j} \left| w_H^{(s_j)}(\theta_{bs}) \right|^2 + \sum_{s_j=1}^L \sum_{s_l=1}^L n_{s_j} n_{s_l} w_H^{(s_j)}(\theta_{bs}) \cdot w_H^{(s_l)*}(\theta_{bs}) (2\pi)^3 H_{s_j s_l}(|\mathbf{k}_{bs} - \text{Re } \mathbf{K}_d|) \right\}. \quad (33)$$

For transforming to the principal frame, the third Stokes parameter has to be calculated. The scattering

from vertical polarization to the third Stokes parameter in the body frame is

$$P_{3_b v_b}(\theta_{bs}, \phi_{bs}; \pi, 0) = \frac{1}{|1-R|^2} \frac{\cos \phi_{bs} \sin \phi_{bs}}{k^2} \cdot 2 \text{Re} \left\{ \sum_{s_j=1}^L n_{s_j} w_V^{(s_j)}(\theta_{bs}) w_H^{(s_j)*}(\theta_{bs}) + \sum_{s_j=1}^L \sum_{s_l=1}^L n_{s_j} n_{s_l} w_V^{(s_j)}(\theta_{bs}) w_H^{(s_l)*}(\theta_{bs}) (2\pi)^3 H_{s_j s_l} \right\}. \quad (34)$$

Scattering from horizontal polarization to the third Stokes parameter in the body frame is

$$P_{3_b h_b}(\theta_{bs}, \phi_{bs}; \pi, 0) = -\frac{1}{|1-R|^2} \frac{\sin \phi_{bs} \cos \phi_{bs}}{k^2} \cdot 2 \text{Re} \left\{ \sum_{s_j=1}^L n_{s_j} w_V^{(s_j)}(\theta_{bs}) w_H^{(s_j)*}(\theta_{bs}) + \sum_{s_j=1}^L \sum_{s_l=1}^L n_{s_j} n_{s_l} w_V^{(s_j)}(\theta_{bs}) w_H^{(s_l)*}(\theta_{bs}) (2\pi)^3 H_{s_j s_l} \right\}. \quad (35)$$

We next transform the phase matrix to the principal frame; for given θ_s and ϕ_s we have

$$\begin{aligned} \sin \theta_s \cos \phi_s \hat{\mathbf{x}} + \sin \theta_s \sin \phi_s \hat{\mathbf{y}} + \cos \theta_s \hat{\mathbf{z}} \\ = \sin \theta_{bs} \cos \phi_{bs} \hat{\mathbf{x}}_b + \sin \theta_{bs} \sin \phi_{bs} \hat{\mathbf{y}}_b + \cos \theta_{bs} \hat{\mathbf{z}}_b. \end{aligned} \quad (36)$$

Thus we can calculate θ_{bs} and ϕ_{bs} in terms of θ_s and ϕ_s by using (36).

Therefore the phase matrix elements in principal frame can be written as

$$P_{VV}(\theta_s, \phi_s; \theta_t, \phi_t = 0) = P_{v_b v_b}(\hat{\mathbf{v}}_s \cdot \hat{\mathbf{v}}_{bs})^2 + P_{h_b v_b}(\hat{\mathbf{v}}_s \cdot \hat{\mathbf{h}}_{bs})^2 + P_{3_b v_b}(\hat{\mathbf{v}}_s \cdot \hat{\mathbf{v}}_{bs})(\hat{\mathbf{v}}_s \cdot \hat{\mathbf{h}}_{bs}), \quad (37)$$

$$P_{HV}(\theta_s, \phi_s; \theta_t, \phi_t = 0) = P_{v_b v_b}(\hat{\mathbf{h}}_s \cdot \hat{\mathbf{v}}_{bs})^2 + P_{h_b v_b}(\hat{\mathbf{h}}_s \cdot \hat{\mathbf{h}}_{bs})^2 + P_{3_b v_b}(\hat{\mathbf{h}}_s \cdot \hat{\mathbf{v}}_{bs})(\hat{\mathbf{h}}_s \cdot \hat{\mathbf{h}}_{bs}), \quad (38)$$

$$P_{VH}(\theta_s, \phi_s; \theta_t, \phi_t = 0) = P_{v_b h_b}(\hat{\mathbf{v}}_s \cdot \hat{\mathbf{v}}_{bs})^2 + P_{h_b h_b}(\hat{\mathbf{v}}_s \cdot \hat{\mathbf{h}}_{bs})^2 + P_{3_b h_b}(\hat{\mathbf{v}}_s \cdot \hat{\mathbf{v}}_{bs})(\hat{\mathbf{v}}_s \cdot \hat{\mathbf{h}}_{bs}), \quad (39)$$

$$P_{HH}(\theta_s, \phi_s; \theta_i, \phi_i = 0) = P_{v_b h_b}(\hat{\mathbf{h}}_s \cdot \hat{\mathbf{v}}_{bs})^2 + P_{h_b h_b}(\hat{\mathbf{h}}_s \cdot \hat{\mathbf{h}}_{bs})^2 + P_{3_b h_b}(\hat{\mathbf{h}}_s \cdot \hat{\mathbf{v}}_{bs})(\hat{\mathbf{h}}_s \cdot \hat{\mathbf{h}}_{bs}). \quad (40)$$

For the passive remote sensing of spherical particles, there is the azimuthal symmetry. The phase function can be calculated by

$$p_{\alpha\beta}(\theta, \theta') = \int_0^{2\pi} d\phi P_{\alpha\beta}(\theta, \phi; \theta', \phi' = 0), \quad (41)$$

where $\alpha, \beta = v, h$.

The scattering coefficient can be calculated by

$$\begin{aligned} \kappa_s &= \int_0^\pi d\theta \sin \theta [p_{vv}(\theta, \theta') + p_{hv}(\theta, \theta')] \\ &= \int_0^\pi d\theta \sin \theta [p_{vh}(\theta, \theta') + p_{hh}(\theta, \theta')]. \end{aligned} \quad (42)$$

The extinction coefficient is $\kappa_e = \kappa_s + \kappa_a$, and the albedo is $\tilde{\omega} = \kappa_s/\kappa_e$. The effective propagation constant K is $K' + i\kappa_e/2$.

The radiative transfer (RT) equations for passive remote sensing are in the following form:

$$\begin{aligned} \cos \theta \frac{dI_v}{dz}(\theta, z) &= -\kappa_e I_v(\theta, z) + \kappa_a CT + \int_0^\pi d\theta' \\ &\cdot \sin \theta' [p_{vv}(\theta, \theta') I_v(\theta', z) + p_{vh}(\theta, \theta') I_h(\theta', z)], \end{aligned} \quad (43)$$

$$\begin{aligned} \cos \theta \frac{dI_h}{dz}(\theta, z) &= -\kappa_e I_h(\theta, z) + \kappa_a CT + \int_0^\pi d\theta' \\ &\cdot \sin \theta' [p_{hv}(\theta, \theta') I_v(\theta', z) + p_{hh}(\theta, \theta') I_h(\theta', z)], \end{aligned} \quad (44)$$

for vertical polarization and horizontal polarization, respectively. Also, $C = K_b K'^2/(\lambda^2 k^2)$ and K_b is the Boltzman's constant.

Consider a two-layer medium (Figure 2); the boundary conditions are the Fresnel type using the effective propagation constant for the dense medium. For the upper boundary, the air-medium 1 interface at $z = 0$,

$$R_v(\theta) = r_v(\theta), \quad (45)$$

$$R_h(\theta) = r_h(\theta), \quad (46)$$

where r_v and r_h are the Fresnel reflectivities with effective propagation constant K .

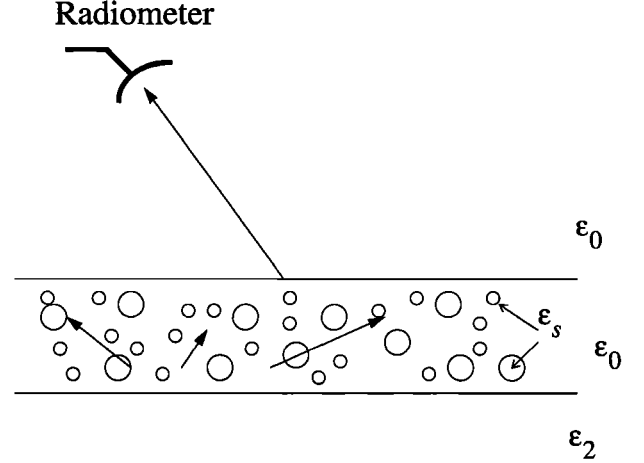


Figure 2. Geometrical configuration for thermal emission from a layer of particles underlying ground.

$$r_v(\theta) = \left| \frac{k^2 \cos \theta - K'(k^2 - K'^2 \sin^2 \theta)^{1/2}}{k^2 \cos \theta + K'(k^2 - K'^2 \sin^2 \theta)^{1/2}} \right|^2, \quad (47)$$

$$r_h(\theta) = \left| \frac{K' \cos \theta - (k^2 - K'^2 \sin^2 \theta)^{1/2}}{K' \cos \theta + (k^2 - K'^2 \sin^2 \theta)^{1/2}} \right|^2. \quad (48)$$

In the lower boundary, the medium 1 and medium 2 interface, $z = -d$,

$$R_{vg}(\theta) = r_{vg}(\theta), \quad (49)$$

$$R_{hg}(\theta) = r_{vg}(\theta), \quad (50)$$

with

$$r_{vg}(\theta) = \left| \frac{\frac{\epsilon_2}{\epsilon_0} k^2 \cos \theta - K' \left(\frac{\epsilon_2}{\epsilon_0} k^2 - K'^2 \sin^2 \theta \right)^{1/2}}{k^2 \cos \theta + K' \left(\frac{\epsilon_2}{\epsilon_0} k^2 - K'^2 \sin^2 \theta \right)^{1/2}} \right|^2, \quad (51)$$

$$r_{hg}(\theta) = \left| \frac{K' \cos \theta - \left(\frac{\epsilon_2}{\epsilon_0} k^2 - K'^2 \sin^2 \theta \right)^{1/2}}{K' \cos \theta + \left(\frac{\epsilon_2}{\epsilon_0} k^2 - K'^2 \sin^2 \theta \right)^{1/2}} \right|^2. \quad (52)$$

The set of RT equations can be solved using the method of Gaussian quadrature [Tsang et al., 1985]. The boundary conditions at the air-snow interface $z = 0$ are

$$I_v(z = 0, \pi - \theta) = R_v(\theta) I_v(z = 0, \theta), \quad (53)$$

$$I_h(z = 0, \pi - \theta) = R_h(\theta)I_h(z = 0, \theta), \quad (54)$$

and for the snow-ground interface $z = -d$, they are

$$I_v(z = -d, \theta) = R_{vg}(\theta)I_v(z = -d, \pi - \theta) + [1 - R_{vg}(\theta)]CT_g, \quad (55)$$

$$I_h(z = -d, \theta) = R_{hg}(\theta)I_h(z = -d, \pi - \theta) + [1 - R_{hg}(\theta)]CT_g, \quad (56)$$

where T_g is the ground temperature.

After solving the eigenvalue problem and imposing the boundary conditions, the brightness temperatures in the direction θ_0 , where $\theta_0 = \sin^{-1}(K' \sin \theta/k)$ is related to θ by Snells' law, are given by

$$T_{B_v}(\theta_0) = \frac{1}{C} [1 - R_v(\theta)]I_v(z = 0, \theta), \quad (57)$$

$$T_{B_h}(\theta_0) = \frac{1}{C} [1 - R_h(\theta)]I_h(z = 0, \theta). \quad (58)$$

4. Pair Distribution Functions and Structure Factors

In applying QCA and QCA-CP the pair distribution function of particle positions must be specified. The Percus-Yevick approximation is used in calculating the particle distribution functions in the study. The pair distribution function measures the probability of finding a particle at \mathbf{r} given a particle at $\mathbf{r} = 0$. The particles are assumed to be nonpenetrable spheres.

4.1. Pair Distribution Functions of Multiple Sizes

In geophysical terrains the particles are of multiple sizes and governed by size distributions. For a system of spherical particles of L different species with radii a_1, a_2, \dots, a_L , respectively, the pair distribution function $g_{ij}(\mathbf{r})$ for a pair of particles of size a_i and a_j is proportional to the probability of finding a particle of size a_j at \mathbf{r} given a particle of size a_i at the origin. For the spherical particles the pair distribution functions g_{ij} are isotropic; that is, $g_{ij}(\mathbf{r})$ depends on $|\mathbf{r}|$ only. Thus $g_{ij}(\mathbf{r})$ can be written as $g_{ij}(r)$. The structure factor $H_{ij}(\mathbf{p})$ also depends on $|\mathbf{p}|$ only. Different approximations have been made to obtain the pair distribution functions by considering the particle positions according to interparticle forces. One of the important results is based on the Percus-Yevick approximation. For the case of general multiple species

the solution is obtained by *Baxter* [1970]. The pair distribution functions are calculated by assuming that the particles are nonpenetrable spheres without interparticle force. The total correlation function $h_{ij}(r)$ is defined as

$$h_{ij}(r) = g_{ij}(r) - 1, \quad (59)$$

where $r = |\mathbf{r}|$. The structure factor $H_{ij}(p)$ is the Fourier transform of $h_{ij}(r)$.

$$\tilde{H}_{ij}(\mathbf{p}) = (n_i n_j)^{1/2} \int d\mathbf{r} e^{i\mathbf{p} \cdot \mathbf{r}} h_{ij}(\mathbf{r}) = (2\pi)^3 H_{ij}(p), \quad (60)$$

where $p = |\mathbf{p}|$. Under the Percus-Yevick approximation, closed-form expressions for $\tilde{H}_{ij}(\mathbf{p})$ are given by *Baxter* [1970].

4.2. Pair Distribution Functions of Sticky Particles

In natural media the densely packed particles can have adhesive force. They adhere together to form aggregates. Thus the model of sticky particles was developed. The sticky particle has a stickiness parameter τ . The smaller the τ is, the more sticky the particles are. The Percus-Yevick approximation of the pair distribution function $g(r)$ for the sticky spherical particles can be solved analytically using the factorization method of *Baxter* [1970]. The calculations of $g(r)$ are given by equations of *Zurk* [1995].

We will study the use of dense media with a single particle size a and with a sticky parameter τ . In Figure 3 the pair functions for several τ are plotted. The scattering depends on the structure factor $H(p)$. In Figure 4 the structure factor $H(p)$ is plotted as a function of pb , where $b = 2a$ is the diameter of the particles, for several τ . For nonsmall τ , that is, for the cases of $\tau = 0.5$ and $\tau = 5$, the interparticle force is small. The usual dense media effect is exhibited. Thus $H(0)$ is negative, indicating that scattering is smaller than independent scattering. On the other hand, for small τ , as shown in the case for $\tau = 0.1$, the interparticle force is strong and $H(0)$ is positive, indicating that scattering is larger than independent scattering for small particles. This is due to the fact that the sticky force creates larger effective particle size at low frequency. We note that in Figure 3, for sticky particles, there are sharp variations of pair functions. These make it difficult to use the Lorentz-Lorenz law to calculate $\text{Im } K$, which is much smaller than $\text{Re } K$. Thus in implementations we use Lorentz-Lorenz law to calculate $\text{Re } K$ but use (42) to calculate κ_s and (10) to calculate κ_a . Then $2 \text{Im } K = \kappa_a + \kappa_s$.

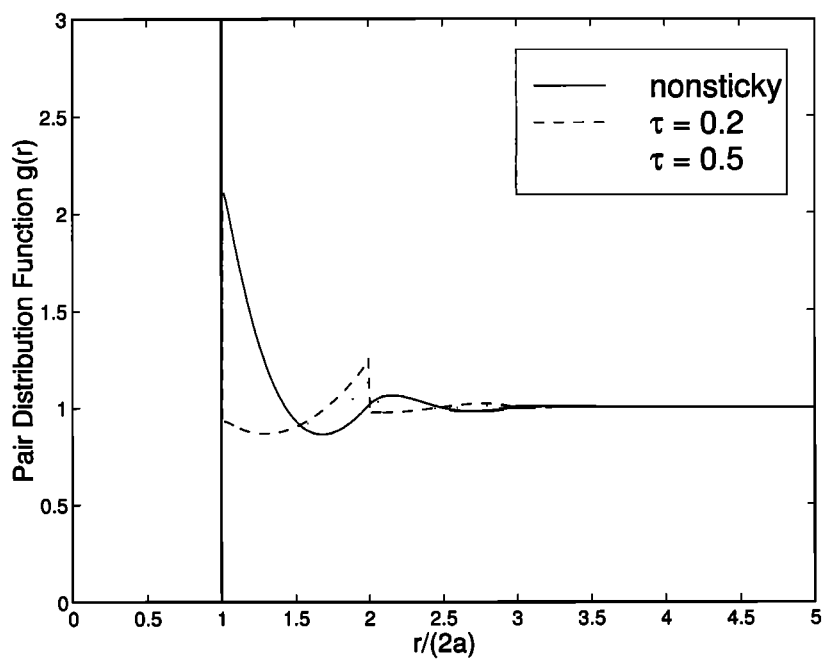


Figure 3. Pair distribution function of sticky particles for various sticky parameters with fractional volume equal to 30%.

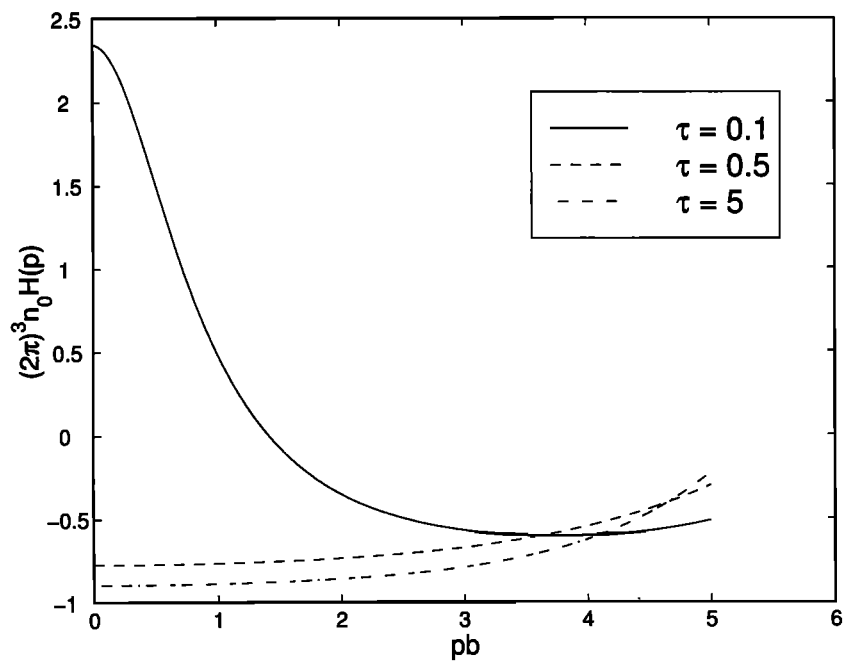


Figure 4. Structure factor $H(p)$ as a function of pb for sticky particles with fractional volume equal to 30%, where b is the diameter of the particles.

Table 1. Numerical Values for the QCA Nonsticky Extinction Rate Calculation

	Species				
	1	2	3	4	5
Diameter, cm	0.05	0.1	0.2	0.3	0.4
Fractional volume	0.1	0.12	0.05	0.02	0.01

Table 2. Numerical Values for the QCA Nonsticky Simulation

	Species	
	1	2
Radius, cm	0.05	0.2
Fractional volume	0.3	0.03
n_0 , cm^{-3}	572	0.89

5. Numerical Simulations of Extinction and DMRT

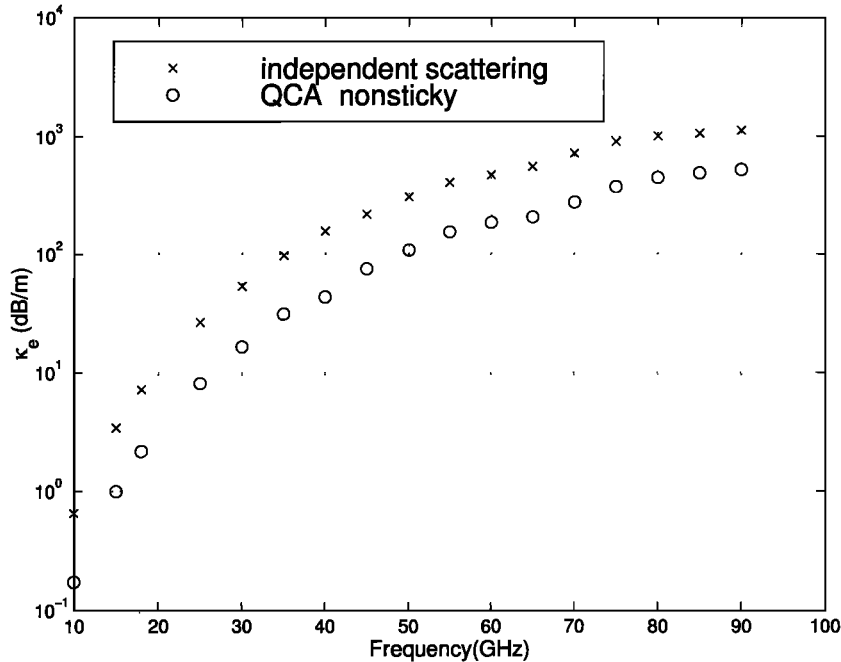
In this section, we illustrate results of multiple-sized nonsticky particles and of the sticky particle model. The effective propagation constant, scattering rate, extinction rate, albedo, and phase functions are first calculated by QCA. These parameters are then put into the RT equations to compute the brightness temperatures.

5.1. Multiple-Sized Nonsticky Particle Model

To analyze the effect of multiple sizes, we first illustrate the use of a medium with particles of five sizes. The size and the fractional volume of each species are listed in Table 1. The relative permittivity of particles is assumed to be $\epsilon_{rs} = 3.2$ for all frequencies. In Figure 5 the extinction rate is plotted

as a function of frequency and compared with the results of independent scattering.

For brightness temperatures calculation we illustrate the use of a medium with particles of two sizes. The size and the fractional volume of each species are listed in Table 2. The first species is of the small particles which occupy a higher volume fraction while the second species is of the large particles. In natural media most of the particles are of small sizes, and only a few particles are large. Assume that the first species has a size of 1 mm in diameter and occupies a volume of 30% while the second species has a size of 4 mm in diameter but only occupies the fractional volume of 3%. The number density ratio is 643. The relative permittivity of particles is assumed to be $\epsilon_{rs} = 3.2 + i0.003$ for both frequencies. The

**Figure 5.** Extinction rate as a function of frequency for multiple moderate-size particles for QCA and independent scattering. Parameters are listed in Table 1.

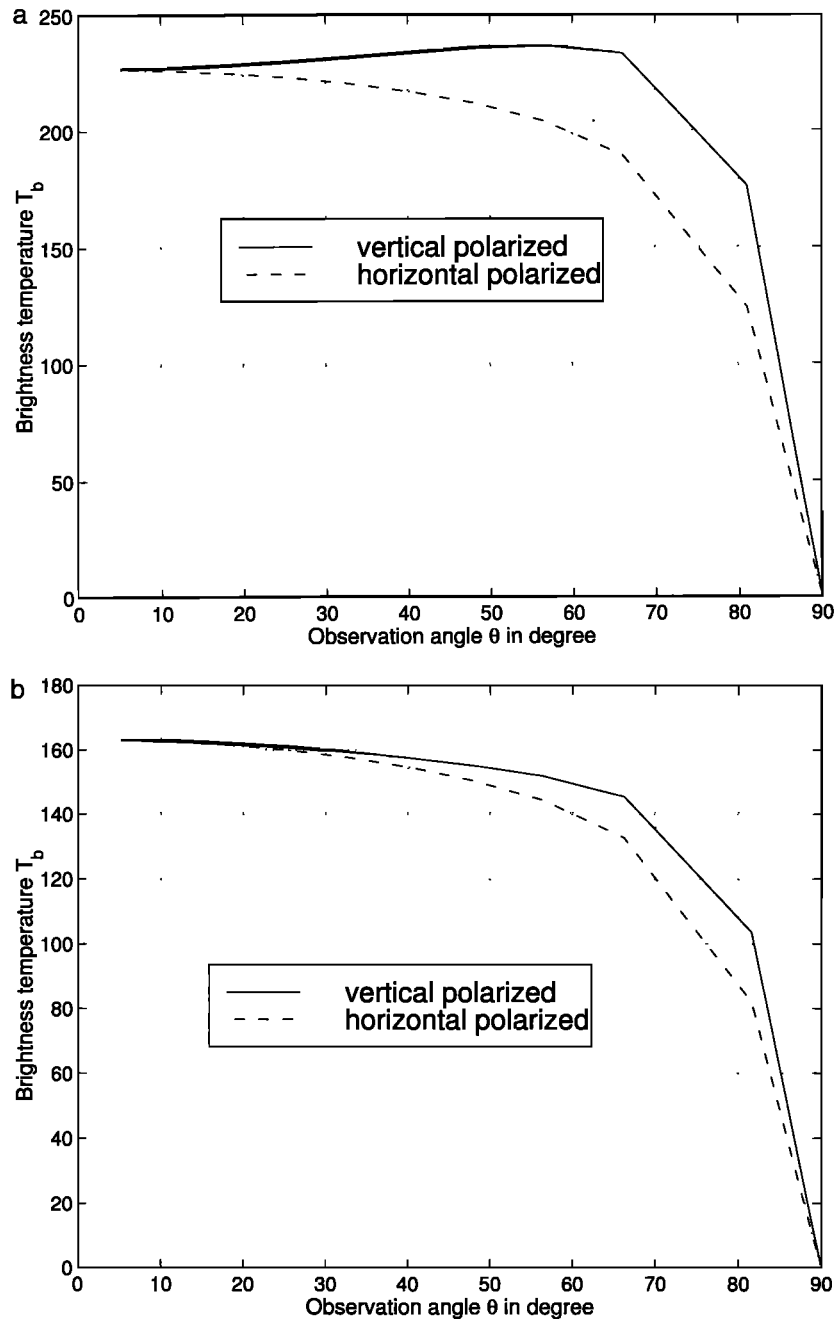


Figure 6. Brightness temperatures versus observation angles based on the no interparticle force model. Medium consists of two particle sizes of 0.1 and 0.4 cm in diameter, with small particles occupying a much larger fractional volume. Parameters are found in Table 2. (a) 19 GHz and (b) 37 GHz.

brightness temperatures for 19 and 37 GHz are presented in Figures 6a and 6b as a function of observation angle. The snowpack physical temperature and the ground temperature are both assumed to

be 270 K. The thickness of the snow layer is 50 cm, and the ground permittivity is $\epsilon_2 = (6 + i0.1)\epsilon_0$. The results indicate that the scattering is important at both frequencies.

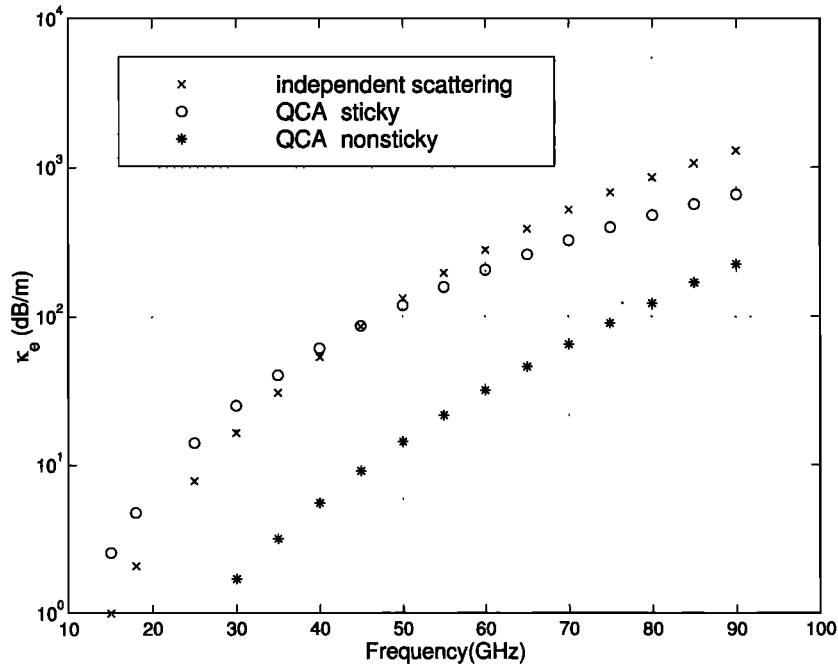


Figure 7. Comparisons of extinction rate as a function of frequency for sticky moderate-size particles of QCA, nonsticky particles of QCA, and independent scattering.

The model of multiple-size particles without inter-particle force exhibits a strong frequency dependence similar to independent scattering. We next study the sticky particle model, which exhibits a weaker frequency dependence.

5.2. Sticky Particle Model

In the sticky particle model the particles are allowed to stick together to form clusters. A single-size sticky particle model is used in this paper. The comparison of the frequency dependence for independent scattering, QCA nonsticky, and QCA sticky is shown in Figure 7. The particle size is 1.2 mm in diameter, and the fractional volume is 30%. The permittivity of the particles is $\epsilon_s = 3.2\epsilon_0$, and the stickiness parameter τ for the sticky particle model is 0.1.

We note that at low frequency the scattering of the QCA sticky model is larger than independent scattering. This is because the particles adhere to form clusters. At low frequencies they scatter like a particle with larger effective size. At high frequency the clustering effect of scattering disappears, and the particles scatter like the usual dense media. Scattering of QCA sticky is less than independent scattering. Thus the frequency dependence of scattering of the

QCA sticky model is less than independent scattering. For the QCA nonsticky model the scattering is less than both independent scattering and the QCA sticky model. For the same particle size the effective size of sticky particle model is larger than that of the non-sticky model. Thus the scattering for QCA sticky is larger than that for QCA nonsticky.

Figure 8 shows the extinction rate as a function of fractional volume. The ratio of the extinction rate between 19 and 37 GHz is ~ 8 –12 times for volume fraction between 0.02 and 0.4. The parameters for the simulation are listed in Table 3. The extinction rate does not increase monotonically as fractional volume. It saturates at fractional volume of 15% and decreases for volume larger than 15%.

After calculating the extinction rate, the scattering rate, and the phase functions by QCA, they are inserted into DMRT equations to calculate the brightness temperatures. Figures 9 and 10 are the calculated brightness temperatures from RT equations based on QCA sticky model and represent typical values in passive remote sensing of snow. In Figure 9 we plot the brightness temperatures of horizontal polarization at 19 GHz as a function of thickness of the scattering layer for various particle

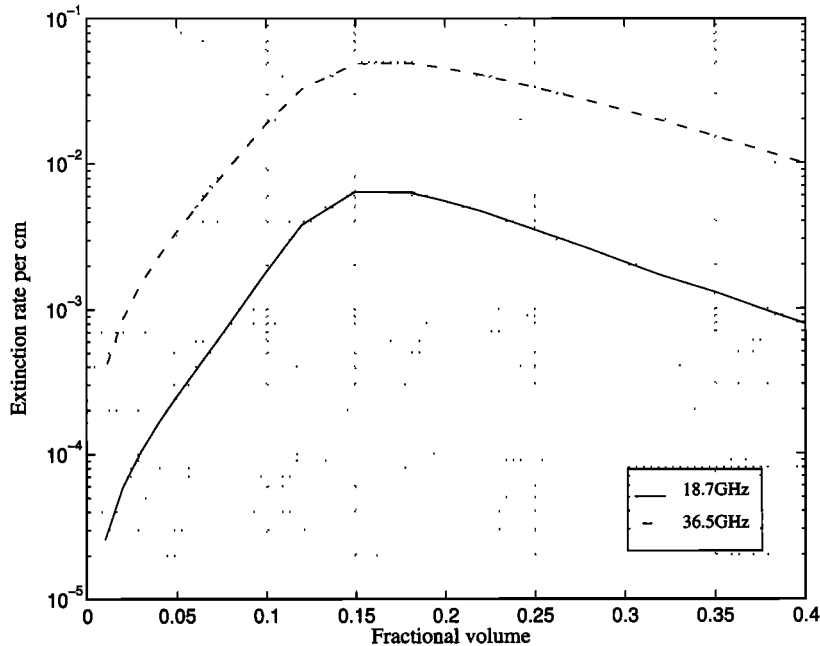


Figure 8. Extinction rate versus fractional volume for 18.7 and 36.5 GHz. The ratio of extinction rate between 18.7 and 36.5 GHz is between 8 and 12 times.

sizes. The observation angle is 55° . In Figure 10 we plot the brightness temperatures for 37 GHz. Figure 11 shows the brightness temperature difference $T_{B19H} - T_{B37H}$. The parameters are listed in Table 4. The brightness temperatures for 19 GHz decrease as layer thickness increases. However, at 37 GHz the brightness temperatures saturate at thickness around 50 cm. This is expectable since the penetration depth for 37 GHz is smaller. The differences of the brightness temperatures (ΔT_B) between two frequencies increase linearly with snow depth at small snow depth and small grain size. For large grain size, because of the saturation at 37 GHz, ΔT_B may even decrease with snow depth as shown in Figure 11. As shown in Figure 11, the mapping between ΔT_B and the thickness is nonunique. The same value of ΔT_B can be

given by two different layer thicknesses depending on the grain size.

6. Data Comparison With SSM/I Measurements Over Snow

In this section, we examine the practicality of the results of the newly developed QCA sticky DMRT model by comparing the results with satellite SSM/I measurements at 19 and 37 GHz. In section 5 the brightness temperatures are calculated by evaluating the volume scattering and absorption of the medium and the snow-air and snow-ground interfaces. Other effects were excluded. In the real-life applications, however, some of the factors have to be taken into account in order to make comparison with satellite SSM/I measurements. Since the emphasis of this paper is on the DMRT model for moderate-size particles, these other factors are included in the solutions in an approximated manner in this section.

In the past approaches of passive remote sensing of snow, investigators often just use $(\Delta T_B)_V$ or $(\Delta T_B)_H$ in the parameter retrievals [Chang *et al.*, 1987]. However, in our approach, we will compare T_B for all four channels 19V, 19H, 37V, and 37H. All four channels contain information of the snow medium.

Table 3. Numerical Values for the QCA Sticky Simulation Shown in Figure 6

Parameter	Value
Diameter, cm	0.06
Stickiness τ	0.1
Relative permittivity of particles	
18.7 GHz	$3.2 + i0.002$
36.5 GHz	$3.2 + i0.01$

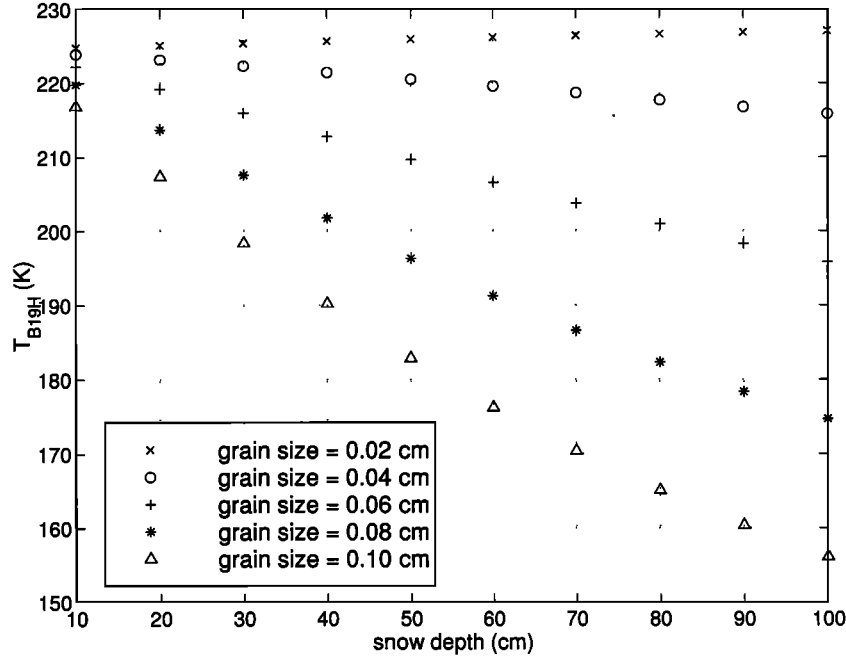


Figure 9. Brightness temperatures of horizontal polarization at 19 GHz as a function of snow depth with various grain sizes based on the sticky particle model with $\tau = 0.1$ and fractional volume equal to 20%. The other parameters are listed in Table 4.

6.1. Roughness Effects

To include the roughness effects of air-snow and snow-ground interface, the reflectivities are modified in the following manner [Wang *et al.*, 1983]:

$$R_v(\theta) = [(1 - Q)r_v(\theta) + Qr_h(\theta)]e^{-H \cos^2 \theta}, \quad (61)$$

$$R_h(\theta) = [(1 - Q)r_h(\theta) + Qr_v(\theta)]e^{-H \cos^2 \theta}, \quad (62)$$

$$R_{vg}(\theta) = [(1 - Q_g)r_{vg}(\theta) + Q_g r_{hg}(\theta)]e^{-H \cos^2 \theta}, \quad (63)$$

$$R_{hg}(\theta) = [(1 - Q_g)r_{hg}(\theta) + Q_g r_{vg}(\theta)]e^{-H \cos^2 \theta}, \quad (64)$$

where Q and H are empirical constants. Q and Q_g are the mixing factor between two polarizations, and H

factor decreases the reflectivity. These reflectivities are used when imposing the boundary conditions described in section 3. The brightness temperatures calculated without atmospheric effects are denoted by T_{B_DMRT} . The emissivity is calculated by setting the snow temperature and the ground temperature to be the same. T_{B0} is the calculated brightness temperature by setting T_g and T_{snow} equal to T without atmospheric effects. The emissivity e is given by

$$e = \frac{T_{B0}}{T}. \quad (65)$$

In this paper, we choose $Q = Q_g = 0.4$ and $H = 1.2$. The relative ground permittivity ϵ_2 is 3.2.

6.2. Atmospheric Effects

The atmosphere is considered as an absorption layer, and an empirical model is used in this paper to include the atmospheric attenuation and emission effects.

The atmosphere is characterized by T_{air} and A . The T_B is thus

$$T_B = AT_{B_DMRT} + T_{\text{air}}(1 - A) + AT_{\text{air}}(1 - A)(1 - e), \quad (66)$$

Table 4. Numerical Values for Figures 9–11

Parameter	Value
Stickiness τ	0.1
Fractional volume	20%
Relative permittivity of particles	
18.7 GHz	$3.2 + i0.002$
36.5 GHz	$3.2 + i0.01$
Snow temperature	260
Ground temperature	260
Relative ground permittivity	3.2

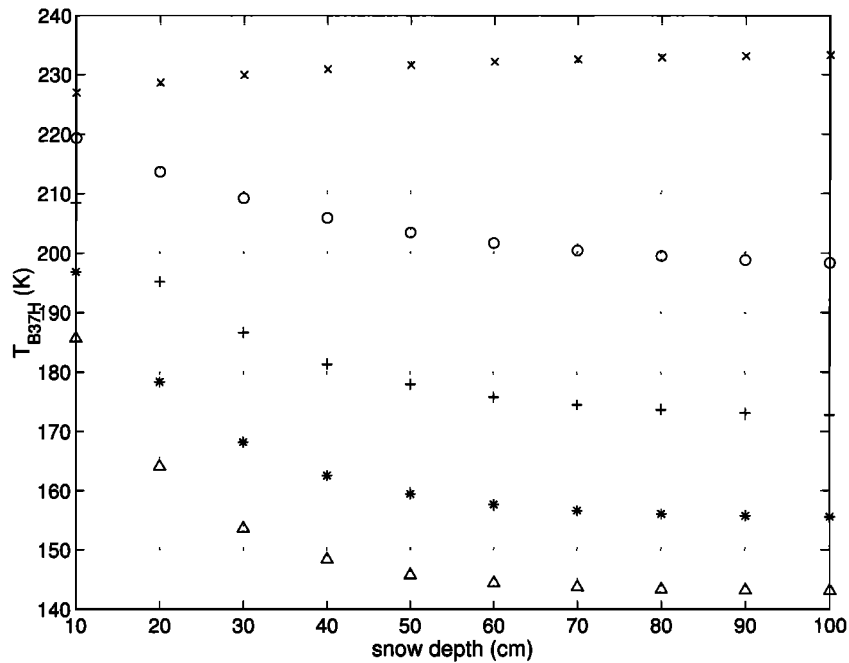


Figure 10. Brightness temperatures of horizontal polarization at 37 GHz as a function of snow depth with various grain sizes based on the sticky particle model with $\tau = 0.1$ and fractional volume equal to 20%. The other parameters are listed in Table 4.

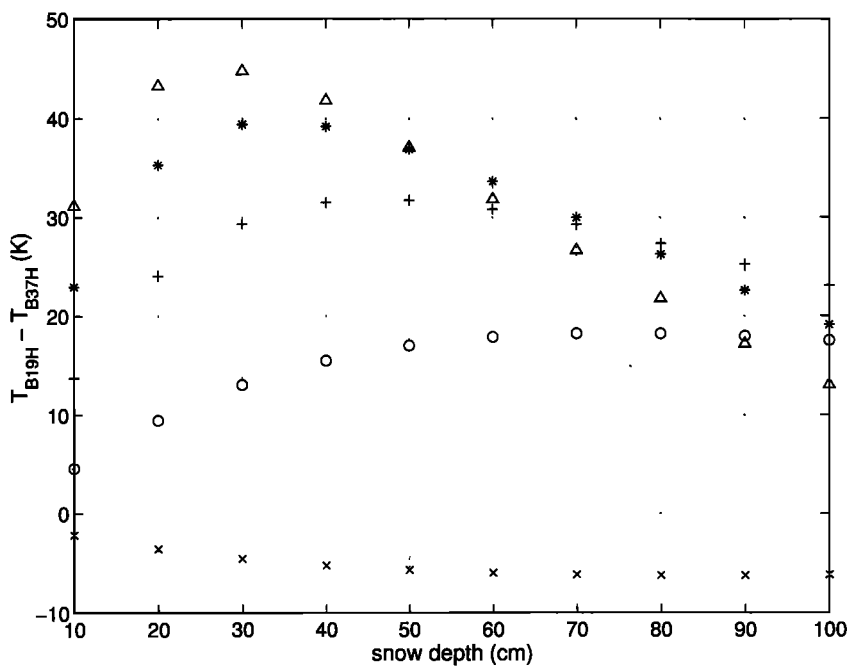


Figure 11. Brightness temperature differences of horizontal polarization as a function of snow depth with various grain sizes based on the sticky particle model with $\tau = 0.1$ and fractional volume equal to 20%. The other parameters are listed in Table 4.

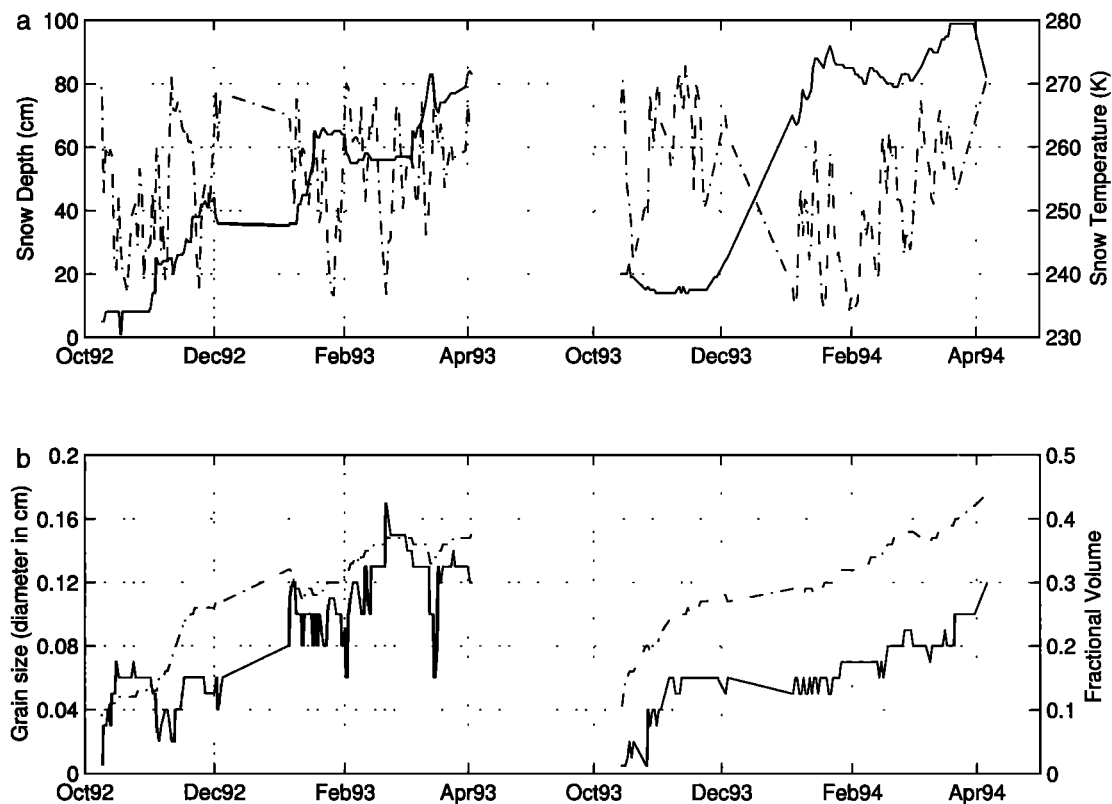


Figure 12. Time evolution of snow depth, snow temperature, grain size, and fractional volume of two snow seasons over the same site. (a) The solid line represents the snow depth, and the dashed line is the snow temperature. (b) The solid line represents the grain size, and the dashed line is the fractional volume.

where $T_{\text{air}} = 250$ K, $A = 0.9225$ for 19 GHz, and $A = 0.8831$ for 37 GHz. Here, e is the emissivity.

The enhancement of the brightness temperatures due to the atmospheric effects for different frequencies will vary. Thus the empirical value A varies with frequencies. The values used in this paper give a maximum enhancement for up to 5 K.

Next we apply the QCA-based DMRT of sticky particles to match data of SSM/I satellite measurements at 19 and 37 GHz for vertical and horizontal polarizations at observation angle of 55° . For applications it is important to match the data as a function of time. The data are taken over the ground station at Pajala (Sweden) with latitude $67^\circ 13' \text{N}$ and longitude $23^\circ 24' \text{E}$. The data are taken over two snow seasons at the same site from July 1, 1992, to June 30, 1994. The ground truth snow depth measurements are available and are plotted in Figure 12a. Comparison between DMRT and the data is made in Figures 13 and 14 for the first and the second snow seasons, respectively. In

calculating DMRT the input parameters that are used are plotted in Figure 12 and listed in Table 5.

We observe the following features in the SSM/I measurements: (1) In the beginning of both snow seasons the brightness temperatures for 19 and 37 GHz are both high, and the differences between the two frequencies are small. This indicates that the snow depth is small. (2) As the season progresses, the brightness temperatures at 19 and 37 GHz both decrease. The brightness temperature differences, however, do not always increase as the snow season progresses. (3) Toward the end of the first snow season the brightness temperatures for 19 and 37 GHz both get really low. However, the differences of the measurements between two channels do not increase as the snow depth increases. However, toward the end of the second snow season the brightness temperatures do not decrease as much as in the first snow season. The differences between the two channels, however, increase with the snow depth. (4)

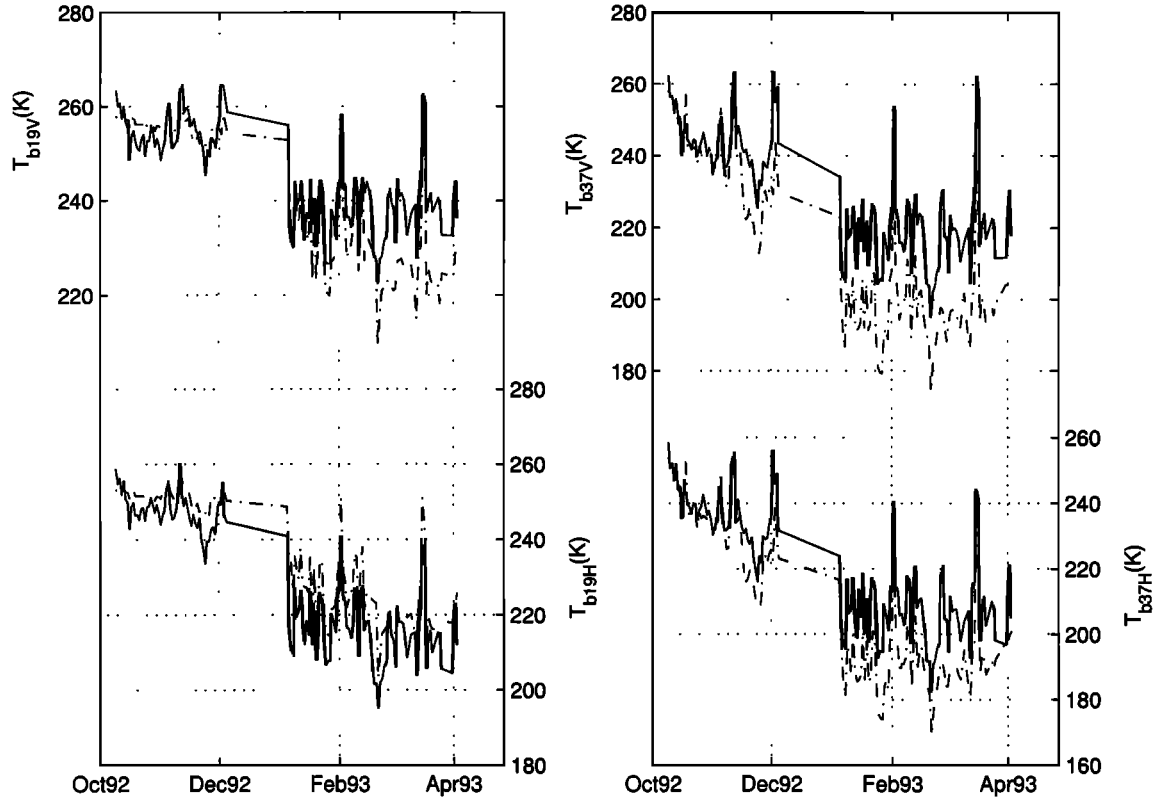


Figure 13. SSM/I brightness temperature measurements and the brightness temperatures calculated by DMRT model for the first snow season. The solid line represents the SSM/I measurements, and the dashed line is the calculated brightness temperatures from DMRT model.

There is a period from early December in 1992 to early January 1993 where no SSM/I data are recorded. This accounts for the abrupt change in the brightness temperature measurements in Figure 13. (5) These two snow seasons over the same site exhibit some major differences. The first snow season, the brightness temperatures have a large decrease as the snow season progresses; the differences between 19 and 37 GHz, however, do not increase as the snow depth increases. (6) If the brightness measurement differences are plotted as a function of ground truth snow depth, there is no clear linear relation. (7) Not only the brightness temperature differences contain information of the snow medium, but also the absolute values of brightness temperatures contain important information.

In selecting the input parameters for the DMRT to match the data, we have chosen the following: (1) For snow depth we use the ground truth measurements. (2) Permittivity for snow grain (ϵ_s) is $3.2(1 + i0.002)$

at 19 GHz and $\epsilon_s = 3.2(1 + i0.01)$ at 37 GHz. The imaginary parts are consistent with measurements [Hallikainen *et al.*, 1987]. (3) Ground permittivity (ϵ_{ground}) is 3.2. This is chosen on the basis of the SSM/I measurements for the small snow depth in the beginning of the snow season. (4) By examining the polarization differences of the SSM/I satellite measurements we choose the mixing factor between two polarizations (Q) to be 0.4 for this study. (5) Ground temperature (T_{ground}) is 270 K. (6) Snow temperatures are given by the snow hydrology model [Wilson *et al.*, 1999; Wigmosta *et al.*, 1994], which uses weather data over the ground station as input. (7) Snow density is also given by the snow hydrology model. (8) Grain size is given by using the snow parameters, such as snow depths, snow temperatures, and snow densities described earlier. We choose the grain size variation to best match all four channels of the SSM/I brightness temperature measurements.

The matching of DMRT model and SSM/I mea-

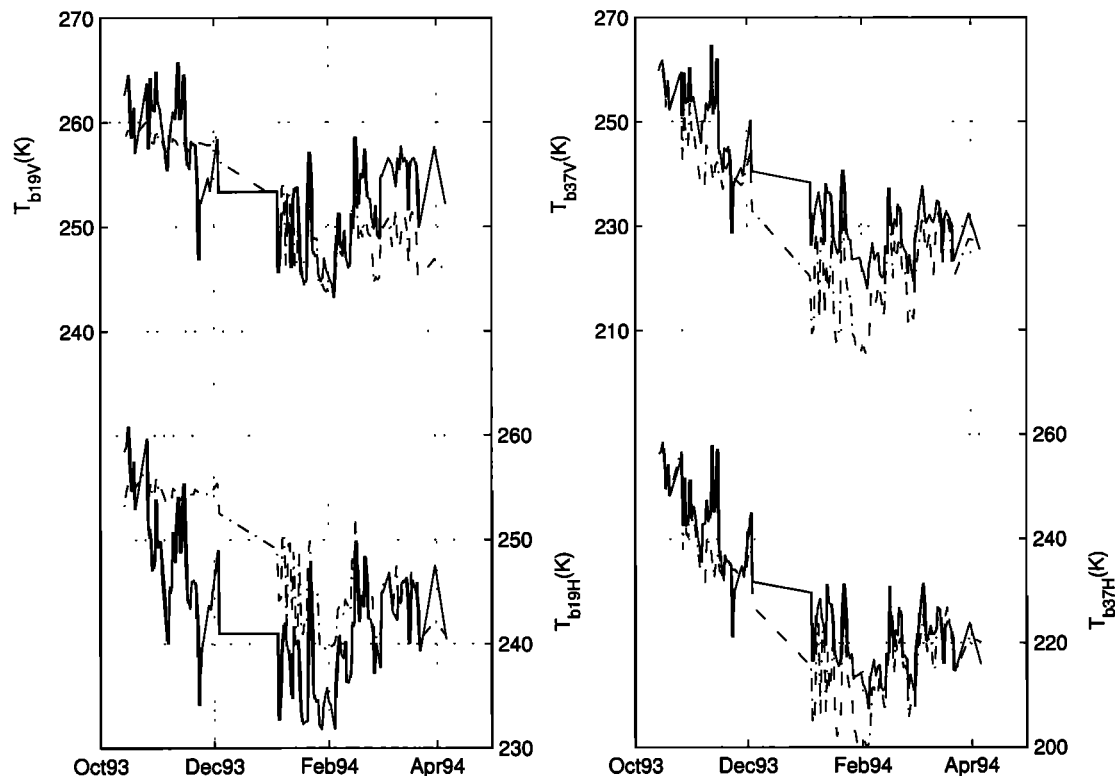


Figure 14. SSM/I brightness temperature measurements and the brightness temperatures calculated by DMRT model for the second snow season. The solid line represents the SSM/I measurements, and the dashed line is the calculated brightness temperatures from DMRT model.

measurements is shown in Figures 13 and 14. The differences between 19 and 37 GHz do not always increase with snow depth. This can be explained by the results of Figure 11. The snow depth and the brightness temperature differences do not have a one-to-one relationship. For a fixed grain size the brightness temperatures at 19 and 37 GHz decrease as the snow depth increases. However, the brightness temperatures for 37 GHz saturate while the brightness temperatures for 19 GHz are still decreasing. This phenomenon is more pronounced for large grain size. The differences between 19 and 37 GHz can decrease with snow depth. Thus the brightness temperatures of

all four channels should be used to obtain the estimates of snow depth.

There are distinct differences between the two snow seasons. For the first snow season the brightness temperatures are low at the end of the snow season. The differences between two frequencies do not always increase with snow depth. For the second snow season the brightness temperatures are not as low as for the first snow season. The differences between the two frequencies increase with snow depth. The phenomenon can be accounted for by a larger grain size in the first snow season and a smaller grain size in the second snow season. Thus, with snow parameters used in DMRT, the brightness temperatures of all four channels as computed by DMRT model match well with SSM/I measurements for two snow seasons.

Table 5. Input Parameters for Data Matching

Parameter	Value
Relative permittivity of particles	
18.7 GHz	$3.2 + i0.002$
36.5 GHz	$3.2 + i0.01$
Ground temperature	270
Relative ground permittivity	3.2

7. Conclusions

In this paper, the quasicrystalline approximation (QCA) for moderate-size particles is studied. Under two different assumptions of interparticle forces, the

QCA nonsticky model and the QCA sticky model are presented. The QCA sticky model exhibits a weaker frequency dependence than independent scattering.

The brightness temperatures can be calculated by inserting the extinction results from the QCA sticky model. For the small particles the differences of brightness temperatures between 19 and 37 GHz have a linear relationship with the snow depth. For the large particles, however, the relation is nonlinear. The brightness temperatures at 37 GHz saturate while the brightness temperatures at 19 GHz still decrease as depth increases; therefore the difference may decrease with snow depth.

To examine the simulation results, cases for two snow seasons are presented. In these two snow seasons the snow depth increases with the same trend. However, the four channels of SSM/I brightness measurements have distinct signatures which can be explained by the sticky particle DMRT model. If only the differences of the brightness temperature are considered, the snow depth cannot be retrieved accurately. The brightness temperatures of all four channels are used in the data matching. The DMRT-calculated brightness temperatures match well with the SSM/I measurements to a snow depth of 1 m.

Acknowledgment. This work is supported in part by NASA contracts NAG5-4739 and NAG5-6495.

References

- Baxter, R. J., Ornstein-Zernike relation and Percus-Yevick approximation for fluid mixtures, *J. Chem. Phys.*, **52**, 4559–4562, 1970.
- Chang, A. T. C., J. L. Foster, and D. K. Hall, Nimbus-7 SMMR derived global snow cover parameters, *Ann. Glaciol.*, **9**, 39–44, 1987.
- Ding, K. H., C. Mandt, L. Tsang, and J. A. Kong, Monte Carlo simulations of pair distribution functions of dense discrete random media with multiple sizes of particles, *J. Electromagn. Waves Appl.*, **6**(8), 1015–1030, 1992.
- Ding, K. H., L. Zurk, and L. Tsang, Pair distribution functions and attenuation rates for sticky particles in dense media, *J. Electromagn. Waves Appl.*, **8**(12), 1585–1604, 1994.
- Hallikainen, M. T., F. T. Ulaby, and T. E. V. Deventer, Extinction behavior of dry snow in the 18- to 90-GHz range, *IEEE Trans. Geosci. Remote Sens.*, **GE-25**(6), 737–745, 1987.
- Ishimaru, A., and Y. Kuga, Attenuation constant of coherent field in a dense distribution of particles, *J. Opt. Soc. Am.*, **72**(10), 1317–1320, 1982.
- Lu, C. C., W. C. Chew, and L. Tsang, The application of recursive aggregate T-matrix algorithm in the Monte Carlo simulations of the extinction rate of random distribution of particles, *Radio Sci.*, **30**(1), 25–28, 1995.
- Tsang, L., Dense media radiative transfer theory for dense discrete random media with spherical particles of multiple sizes and permittivities, in *Progress in Electromagnetics Research*, vol. 6, *Dielectric Properties of Heterogeneous Materials*, edited by A. Priou, chap. 5, pp. 181–230, Elsevier Sci., New York, 1992.
- Tsang, L., and J. A. Kong, Scattering of electromagnetic waves from a dense medium consisting of correlated Mie scatterers with size distributions and applications to dry snow, *J. Electromagn. Waves Appl.*, **6**(3), 265–286, 1992.
- Tsang, L., J. A. Kong, and R. Shin, *Theory of Microwave Remote Sensing*, Wiley-Interscience, New York, 1985.
- Tsang, L., C. E. Mandt, and K. H. Ding, Monte Carlo simulations of the extinction rate of dense media with randomly distributed dielectric spheres based on solution of Maxwell's equations, *Opt. Lett.*, **17**(5), 314–316, 1992.
- Wang, J. R., P. E. O'Neill, T. J. Jackson, and E. T. Engman, Multi-frequency measurements of the effects of soil moisture, soil texture and surface roughness, *IEEE Trans. Geosci. Remote Sens.*, **GE-21**(1), 44–51, 1983.
- Wigmosta, M., L. Vail, and D. P. Lettenmaier, A distributed hydrology-vegetation model for complex terrain, *Water Resour. Res.*, **30**, 1665–1679, 1994.
- Wilson, L., L. Tsang, J.-N. Hwang, and Chi-Te Chen, Mapping snow water equivalent in mountainous areas by combining a spatially distributed snow hydrology model with passive microwave remote sensing data, *IEEE Trans. Geosci. Remote Sens.*, **37**(2), 690–704, 1999.
- Zurk, L., Electromagnetic wave propagation and scattering in dense, discrete random media with application to remote sensing of snow, Ph.D. dissertation, Univ. of Washington, Seattle, 1995.
- A. T. C. Chang, Hydrological Sciences Branch, NASA Goddard Space Flight Center, Greenbelt, MD 20771-0001.
- C.-T. Chen, J. Guo, and L. Tsang, Department of Electrical Engineering, University of Washington, Box 352500, Seattle, WA 98195-2500.
- K.-H. Ding, Air Force Research Laboratory, Sensors Directorate/SNHE, 800 Scott Road, Hanscom AFB, MA 01731-2909.

(Received October 12, 1999; revised February 28, 2000; accepted March 7, 2000.)